Trends in the CO oxidation and PROX performances of the platinum-group metals supported on ceria

T. S. Nguyen, F. Morfin, M. Aouine, F. Bosselet, J. L. Rousset, L. Piccolo

Trends in the CO oxidation and PROX performances of the platinum-group metals supported on ceria

Thanh-Son Nguyen, Franck Morfin, Mimoun Aouine, Françoise Bosselet, Jean-Luc Rousset, and Laurent Piccolo*

Institut de recherches sur la catalyse et l'environnement de Lyon (IRCELYON), UMR 5256 CNRS & Université Lyon 1, 2 avenue Albert Einstein, F-69626 Villeurbanne, France

Abstract: PGM-CeO_2 (PGM = Pt, Pd, Ir, Rh, Ru) catalysts were prepared by one-step solution combustion synthesis (SCS) and characterized by elemental analysis, N_2 volumetry, aberration-corrected HRTEM, X-ray diffraction, and CO-DRIFTS. The samples, consisting of 2-6 nm metal nanoparticles supported on mesoporous ceria, were tested in CO oxidation in absence and presence of hydrogen (PROX). To our knowledge, this work presents the first comparison of all the platinum-group metals (except Os) for these reactions in the same conditions. The as-prepared SCS catalysts are active in CO oxidation and a reducing treatment has no significant effect on their performances. While the best catalyst in H_2-free CO oxidation is Rh-CeO_2, the addition of a high hydrogen excess decreases the Rh catalyst activity but enhances the CO oxidation rate on all other systems, including alumina-supported ones. The resulting PROX turnover frequencies (Pt > Pd > Rh > Ir > Ru) follow the trends predicted by published density-functional-theory calculations considering the CO_{ad}+O_{ad} elementary reaction as the rate-determining step. Pt-CeO_2 is not only the most active but also the most selective catalyst, reaching near 100% CO_2 at low temperature (ca. 100 °C). The ceria-supported Pt, Pd and Ir catalysts were compared with their alumina-supported counterparts, which appeared less active in both reactions. The effect of heating/cooling cycles on the reaction kinetics was also investigated. Whereas the Pt, Pd and Ir catalysts were stable throughout PROX cycles, Rh and Ru exhibited apparently chaotic behaviors above ca. 200 °C, which are proposed to be induced by favorable CO dissociation and methanation pathways and/or variable metal oxidation states.

Keywords: CO oxidation; PROX; Methanation; Platinum-group metals; Ceria; Solution combustion synthesis

* Corresponding author: laurent.piccolo@ircelyon.univ-lyon1.fr. Phone: +33 472 445 324

1. Introduction

Beyond the prototypical catalytic oxidation of CO, the preferential oxidation of CO in hydrogen excess (PROX) has been proposed as a viable process to remove CO impurities from reformate hydrogen, in order to feed onboard proton-exchange-membrane fuel cells with pure hydrogen and thereby avoid the Pt anode poisoning by CO [1–3]. PROX has been widely studied over platinum-group metals (PGMs, i.e. Pt, Pd, Ir, Rh, Ru, and Os) supported on non-reducible oxides (typically Pt/Al_2O_3), and coinage metals supported on reducible oxides (typically CuO/CeO_2). Conversely, the combination of PGMs with reducible oxides has been much less studied, although reducible oxides are known to act as PGM promoters in PROX [3]. Due to its excellent redox properties, ceria is extensively used in heterogeneous catalysis, where it can act as an oxygen buffer for oxidation reactions [4]. The three-way catalytic converter for gasoline-powered automotive engines is the best known catalytic application of ceria. It typically consists of a monolith washcoated with a ceria-zirconia/alumina film containing Pt, Pd, and Rh nanoparticles, which are active for catalyzing CO/hydrocarbon oxidation and NOx reduction. Both for CO oxidation and PROX, ceria has proved its superiority over any other simple oxide as a PGM support, especially at low temperatures [5–7]. This is explained by the existence, in addition to the standard Langmuir-Hinshelwood mechanism which proceeds on the metal only, of a second mechanism involving oxygen from ceria at the metal/ceria interface [5,8].

To the best of our knowledge, there has been no report to date comparing, under the same conditions, the PGM/ceria series in CO oxidation or PROX. Only Mariño et al. compared Pt, Pd, and Ir on various oxides, including ceria, showing the following hierarchy between the studied metals in terms of PROX performances: Pt > Ir >> Pd [6]. Rh and Ru-based catalysts have been rarely studied for PROX. Galletti *et al*. investigated a Rh/CeO_2 catalyst [9], and Chen *et al*. studied a Ru/Al_2O_3 catalyst modified by ceria–terbia mixed oxide [10]. $Ru(Ce_{0.8}Tb_{0.2}O_2)/Al_2O_3$ performs well, whereas Rh/CeO_2 is not compelling for PROX. Oh and Sinkevitch compared various commercial catalysts for application of PROX to fuel cells and reported that Ru/Al_2O_3 and Rh/Al_2O_3 are more selective than Pt/Al_2O_3 [11].

In this paper, we compare all the PGMs (except Os, which forms a highly toxic oxide in ambient air) supported on ceria for CO oxidation and PROX. In addition to metal benchmarking for each reaction, we emphasize the strongly metal-dependent (positive or negative) effect of hydrogen on CO oxidation activity. Moreover, we also assess the support effect using a commercial Pt/Al_2O_3 catalyst as reference and previous results for Pd/Al_2O_3 and Ir/Al_2O_3. For catalyst preparation, we have used solution combustion synthesis (SCS), which consists in the fast and self-sustained combustion of a pre-heated aqueous solution of a metallic salt (usually nitrate) and an organic fuel (typically glycine) [12]. Unlike for mixed oxides, SCS has been very scarcely used for the preparation of noble metals/oxides

combinations [9,13–15]. Here, this method has been employed to prepare a PGM/ceria series with the objective of maximizing the metal dispersion and the metal-oxide interaction, while limiting metal-dependent nanoparticle size issues inherent to conventional impregnation methods.

2. Experimental

2.1. Catalyst preparation

A series of CeO_2 and PGM-CeO_2 powders (see Table 1) was prepared by solution combustion synthesis (SCS), using ceric ammonium nitrate, CAN [$(NH_4)_2Ce(NO_3)_6$, Sigma-Aldrich, 99.99%] as both ceria precursor salt and oxidizing agent. The PGM precursors were: $H_2PtCl_6.6H_2O$ (Strem Chemicals, 38-40% Pt), $Pd(NH_3)_4Cl_2.H_2O$ (Sigma-Aldrich, 98%), $(NH_4)_2IrCl_6$ (Strem Chemicals, 99%), $RhCl_3$ (Sigma-Aldrich, 38-40% Rh), and $RuCl_3$ (Sigma-Aldrich, 38-42% Ru). Glycine ($C_2H_5NO_2$, Sigma-Aldrich, 99%) was used as fuel. The CAN:glycine:PGM precursor mixture composition was chosen in order to obtain stoichiometric proportions of oxidizer and fuel (*i.e.*, with the oxidizing/reducing valence ratio of the redox mixture equal to 1) [16] and reach the desired metal loading (1 wt%). Table 1 shows the actual loadings.

Practically, a borosilicate beaker (300 cm^3) containing a mixture of CAN (5.00 g), glycine (1.82 g), PGM precursor, and 30 mL deionized water was introduced into a muffle furnace (Carbolite ELF 11/6) maintained at 350 °C. At the point of complete dehydration (5-10 min), the solution started boiling and foaming, and ignition took place after a few seconds with rapid evolution of a large quantity of gases. This yielded a voluminous solid product within a few minutes. The powder color ranged from pale yellow (CeO_2) to brown-grey (PGM-CeO_2).

2.2. Catalyst characterization

The metal amounts were determined by inductively coupled plasma - optical emission spectroscopy (ICP-OES, Activa instrument from Horiba Jobin Yvon). In order to dissolve them completely, the samples were treated with a mixture of H_2SO_4, royal water and HF at 250-300 °C.

Isotherm determination was performed by N_2 adsorption volumetry at -196 °C (ASAP 2010M instrument from Micromeritics). Specific surface areas were derived using the BET method. Prior to the measurements, the powders were outgassed at 300 °C for 2 h in vacuum.

The crystalline structure was analyzed at RT and ambient atmosphere using a Bruker D8 Advance A25 diffractometer (Cu Kα radiation at 0.154184 nm) equipped with a Ni filter and 1-D fast multistrip detector (LynxEye, 192 channels on 2.95°). The diffractograms were collected at 2θ with steps of 0.02 ° from 4 to 80 ° for a total acquisition time of 32 min and from 20 to 85° for a total acquisition time of 110 min. Phase identification was performed using the Diffrac.Eva software (Bruker) and the ICDD-PDF4+ database. The lattice parameters and the crystallite sizes were determined using the Rietveld method (Fullprof code).

The local sample microstructure was examined by high-resolution transmission electron microscopy (TEM) and scanning transmission electron microscopy – high angle annular dark field (STEM-HAADF) using a FEI Titan G2 aberration-corrected ETEM (in high-vacuum mode) operated at 300 kV with 1 Å best resolution. The samples were crushed in ethanol and the solution was ultrasonically stirred before dropping it on a holey carbon-covered copper TEM grid, followed by drying. In some cases, a standard reducing pretreatment consisting in heating the as-prepared samples to 400 °C (5 °C min^{-1}, 2 h plateau) in pure H_2 flow (3-7 L h^{-1}, 1 atm), was applied. This temperature was found high enough for reducing all the metals while avoiding an extensive reduction of ceria, which can be detrimental for the catalytic performances [17]. For example, CO oxidation tests performed after reduction at 500 °C on Pt-CeO_2 showed a slight decrease in activity as compared to the 400 °C reduction case (not shown).

Infrared spectroscopy of adsorbed CO was performed using a Thermo Nicolet 6700 FTIR spectrophotometer equipped with an *in situ* diffuse reflectance infrared Fourier Transform spectroscopy (DRIFTS) chamber (Harrick HVC-DRP cell) and a high-sensitivity MCT detector. The cell was connected to a gas handling system allowing for *in situ* treatments with several gases at temperatures up to 500 °C. About 30 mg of the powder sample was placed into the cell sample holder and pretreated under He flow (40 mL min^{-1}, 1 atm) at 300 °C for 1 h. CO was pre-adsorbed by exposing the sample kept at 50 °C to a flow of 1% CO in He for 15 min. Then the CO+He feed was replaced with pure He, and a spectrum was acquired at 50 °C. For *in situ* reduction, the sample was exposed to a flow of pure H_2 at 400 °C for 1 h. The spectra were recorded in the 650-4000 cm^{-1} range at a resolution of 2 cm^{-1} by accumulating 128 scans. The Omnic software (Thermo) was used for initial data processing.

2.3. Catalyst evaluation

Each catalyst was evaluated in two reactions: the oxidation of CO and the preferential oxidation of CO in H_2 excess (PROX). These tests were carried out at atmospheric pressure and variable temperature in a continuous flow fixed-bed reactor. The catalysts were diluted in Al_2O_3 (Condea Puralox ScFa-215)

in order to obtain a catalytic bed of 800 mg (13 mm height in a quartz U-shaped 10 mm-diameter tubular reactor). The reactant gases were mixed using mass-flow controllers (Brooks Instruments) and flowed through the reactor at a total rate of 50 NmL min^{-1}. All the high-purity (> 99.995%) gases were purchased from Air Liquide. The gas mixture consisted of 2% CO + 2% O_2 + 96% He for CO oxidation, and 2% CO + 2% O_2 + 48% H_2 + 48% He for PROX. The outlet gases were analyzed online using a Varian MicroGC (CP2003).

The following standard test sequence was used (unless specified) for the catalytic tests: CO oxidation, *in situ* reducing treatment, CO oxidation, and PROX. The pretreatment consisted in heating the catalyst under hydrogen flow (50 ml min^{-1}) from room temperature (RT) to 400 °C at a rate of 3 °C min^{-1}, followed by 2 h plateau at 400 °C. The CO oxidation and PROX experiments consisted of two heating-cooling cycles (50-350-50°C) at a rate of 80 °C h^{-1}.

3. Results

3.1. Catalyst composition and structure

N_2 volumetry. The BET specific surface areas are in the 12–35 m^2/g range (Table 1). The N_2 physisorption isotherms, as those shown in Fig. S1 (Supplementary Data file) for Pd-CeO_2 and Rh-CeO_2, are of type IV with a H3 hysteresis loop and quasi vertical parallel branches at high pressure [18]. Although the BET area varies from one catalyst to the other, the isotherms all display the same shape and only differ by the width of the hysteresis loop: the higher the area, the wider the loop. As seen in Fig. S1, the isotherm of Rh-CeO_2, the catalyst with the lowest surface area (12 m^2/g), is close to type II with a very thin H3 hysteresis loop. These features are consistent with mesoporous materials with broad pore size distribution, containing aggregates of plate-like particles giving rise to slit-shaped pores, and substantial external surface [18].

X-ray diffraction. From XRD (Fig. S2), the SCS-prepared materials exhibit the fluorite structure of standard CeO_2 (space group Fm-3m, #225). From Table 1, the ceria lattice parameter appears slightly dependent on the PGM nature. It is comprised between 5.412 and 5.415 Å. As the PGM ionic radii are smaller than the Ce ones [19], the slight increase in lattice parameter with respect to ceria (from ICDD database, the standard value is 5.411(2) Å for stoichiometric CeO_2) observed for Pd, Ir, Rh, and Ru samples, cannot be related to metal insertion into the ceria lattice. In fact, on the basis of XRD data, such an insertion can be neither proved nor excluded. Indeed, the metal loadings are too low to induce a significant change in the ceria lattice parameter. Instead, the increase of this parameter is ascribed to the presence of Ce^{3+}, the ionic radius of which is bigger than the Ce^{4+} one (1.14 Å *vs.* 0.97 Å for

coordination 8) [20]. In the case of Ir-CeO_2, the somewhat high value of the lattice parameter (5.415 Å) was already ascribed by some of us to the partial reduction of the ceria surface induced by the strong interaction between Ir and CeO_2 [15].

Electron microscopy. Figure 1 gives an overview of the micro and nano-structure of the combustion-synthesized ceria-based samples from TEM observations. Since the detailed structures of Ir-CeO_2 and Ru-CeO_2 are or will be reported elsewhere [15,17,21], only images of Pt-CeO_2, Pd-CeO_2, and Rh-CeO_2 are shown here. However, for a given fuel, the texture and structure of ceria grains essentially does not depend on the presence and nature of the metal [15,21]. The spongy texture clearly visible in Figure 1d is typical of SCS materials, the fast evolution of gases during the highly exothermic combustion giving rise to round macropores. At smaller scale, the puzzle-like structure (clearly visible in Fig. 1g for Rh-CeO_2) is also characteristic of combustion-synthesized ceria, and was observed in most cases. The HRTEM images, which contain Moiré patterns (Fig. 1h) and stacked features (Fig. 1i), suggest a flat layered structure, consistently with the shape of the physisorption isotherms (Fig. S1). While the as-prepared ceria surface appeared amorphous (Fig. 1, b and c), the treatment in H_2 at 400 °C led to flat and facetted edges or surfaces (see Fig. 1i for Rh-CeO_2), ascribed to ceria surface cleaning and recrystallization. Metal nanoparticles in the size range of 2-6 nm (see Table 1, Table S1, and Fig. S3) were observed at the surface of ceria grains (see Fig. 1a-c for Pt and Fig. 1g-i for Rh). Note that as-prepared samples also exhibit nanoparticles, as shown for Pt-CeO_2 in Figure 1a.

Infrared spectroscopy. In order to determine the oxidized or metallic nature of the PGM surface phases and the effect of the reducing pretreatment (400 °C, H_2 flow), as-prepared and reduced materials were characterized by CO-DRIFTS at 50 °C under He flow, after exposure to 1% CO + He flow. The results are presented in Figure 2.

Bare ceria, whether fresh or reduced, does not show any indication of CO adsorption [22]. The absence of CO adsorption on the reduced sample is ascribed to the small extent of ceria reduction after treatment at 400 °C [15] and/or the mild measurement temperature (50 °C). Overall, the fresh PGM catalysts adsorb CO in small amounts. Conversely, after catalyst heating in H_2, strong infrared absorption bands due to C-O stretching vibrations are visible. In the case of Pt, the band at 2108 cm^{-1} is ascribed to CO adsorption on Pt oxide. Upon reduction, a strong band centered at 2070 cm^{-1} appears, which is due to CO linearly adsorbed on Pt^0 [23–26]. The shoulder around 2108 cm^{-1} suggests that part of the Pt remains oxidized. A smaller band at 1844 cm^{-1} is ascribed to bridged CO adsorption. The spectrum structure is more complex for Pd. Linear (~2090 cm^{-1}) and bridged (~1960 cm^{-1}) CO-Pd^0 species are present, both on fresh and reduced materials [27,28]. The band at 2147 cm^{-1} suggests the presence of oxidized Pd in the as-prepared catalyst. For Ir, the band centered at 2046 cm^{-1} is due to

linear adsorption of CO on the metal, while the low-frequency tail can be ascribed to bridge-bonded CO [15,29–31]. In the case of Rh, the two bands at 2086 and 2015 cm^{-1} correspond to coupled C-O stretching vibration modes of *gem*-dicarbonyl $Rh^{I}(CO)_2$ species, associated to highly dispersed Rh [32–34]. Finally, the fresh Ru catalyst exhibits significant adsorption bands at around 2060, 1981, and 1839 cm^{-1}. We ascribe the two formers to multicarbonyl CO species adsorbed on metallic or partially oxidized Ru, although the literature is contradictory on the assignments [35–38]. The 1839 cm^{-1} band corresponds to bridge or ternary CO adsorbed on Ru, or, alternatively, to an overtone of supported RuO_2. After the reducing treatment, this feature disappears while the multicarbonyl bands increase in intensity and a small band at 2163 cm^{-1}, tentatively ascribed to $Ru^{\delta+}$-CO monocarbonyls, appears. In conclusion of this part, the thermal treatment in H_2 leads to a high extent of PGM oxide reduction and the formation of metal nanoparticles at the surface of mesoporous ceria.

3.2. Catalyst performances

All the samples were submitted to the same testing procedure, consisting in (i) a first series of two heating/cooling CO oxidation cycles (4 reaction runs), starting from the as-synthesized catalyst; (ii) a reduction in H_2 at 400 °C; (iii) a second series of two CO oxidation cycles (4 runs); (iv) a series of two PROX cycles (4 runs). In one case (Rh-CeO_2), a further reduction at 400 °C and two additional PROX cycles, with 210 °C maximum temperature, were applied (see below). For comparison purposes, a commercial 0.95 wt% Pt/Al_2O_3 catalyst (Sigma-Aldrich) was tested in the same conditions. Figure 3 shows the full set of data (CO_2 yields), which highlights the cycling behaviors of the catalysts, while Figures 4 and S4 allow comparing the catalyst activities and selectivities based on the last CO oxidation and PROX runs. In order to derive turnover frequencies (TOFs), the activities were normalized over the number of surface metal atoms. To this purpose, for each sample the metal dispersion was calculated from $\alpha/\langle d \rangle_{surf}$, where $\alpha = 6 v_m n_s$ with v_m being the volume occupied by an atom in bulk metal, n_s the mean number density of surface atoms, and $\langle d \rangle_{surf}$ the surface-weighted mean particle diameter obtained from the TEM particle size distribution (see Table S1 and Fig. S3). With $\langle d \rangle_{surf}$ expressed in nm, α = 1.1 for fcc Pt, Pd, Ir and Rh metals, and 1.3 for hcp Ru. This formula is valid for roughly spherical PGM nanoparticles exhibiting low-index facets [39,40].

CO oxidation. Regarding CO oxidation, comparing run 1 to run 3 (increasing temperatures) during the first reaction series (as-prepared catalysts), Pt and Pd show a slight deactivation (variation of the temperature at half-conversion $\Delta T_{1/2}$ = +15 °C) while Rh and Ru show a small activation ($\Delta T_{1/2}$ = -28 and -8 °C, respectively) and Ir is stable (Fig. 3). The subsequent reduction has a negligible influence on Pt, Pd, and Ru catalysts, while it induces a slight deactivation of Ir-CeO_2 ($\Delta T_{1/2}$ = +16 °C) and a more

significant deactivation of Rh-CeO_2 ($\Delta T_{1/2}$ = +30 °C), suggesting either higher activity of the oxidized Ir and Rh phases or poisoning of the sample at high temperature (see Section 4.1). One can conclude from these cycling experiments that, unlike conventional catalysts prepared by impregnation [21], the fresh SCS catalysts do not need any activation pretreatment. Only in the case of Rh-CeO_2, the first heating in the CO oxidation mixture leads to the (slightly) highest reaction rate with respect to other runs. Besides, it can be noted that the Pd and Pt catalysts have very similar behaviors in any conditions.

Figure 4a shows the CO_2 yields in the case of the last CO oxidation runs (series 2/run 4). Figure 4b (open symbols) allows establishing the following order in terms of TOF: Rh > Pd > Pt > Ru > Ir. At 140 °C, the CO_2 formation TOF varies from 0.01 s^{-1} (Ir) to 1.0 s^{-1} (Rh). As shown by Table 2, the apparent activation energies range between 45 kJ/mol (Pd) and 90 kJ/mol (Ru).

Finally, as seen in Figure 4a, the replacement of alumina with ceria support for Pt somewhat decreases the light-off temperature. As a result, at 150 °C, the CO oxidation activity per metal weight is multiplied by 3.5 (Fig. S4). A similar conclusion can be drawn for Pd and Ir when comparing the present results with those previously obtained in the same conditions using alumina as support (Fig. S5). These experiments made use of 0.81 wt% Pd/Al_2O_3 (Pd particle size 3.1 ± 1.4 nm) and 0.80 wt% Ir/Al_2O_3 (Ir particle size 1.4 ± 0.3 nm) prepared by incipient wetness impregnation [41].

PROX. Figures 4c and 4d show the CO_2 yields and the corresponding selectivities to CO_2 in the last PROX runs (series 3/run 4), respectively. The addition of hydrogen to the CO+O_2 mixture has a promoting effect on the activity of all the catalysts (including pure ceria), except Rh-CeO_2. The strongest promotion is obtained for Pt-CeO_2, with an overall decrease of $T_{1/2}$ by 120 °C. The resulting TOF order is the following: Pt > Pd > Rh > Ir > Ru (Arrhenius plot of Fig. 4b, filled symbols). At 140 °C, the CO_2 formation TOF varies from 0.06 s^{-1} (Ru) to 3.3 s^{-1} (Pt). As shown by Table 2, the apparent activation energies vary between 59 kJ/mol (Pd) and 92 kJ/mol (Ru), and the changes from CO oxidation values are strongly metal-dependent. In addition, from Pt/Al_2O_3 to Pt-CeO_2, a considerable increase in activity is measured. For example, at 100 °C, the activity per metal weight is multiplied by 36 (Fig. S4). An increase in CO PROX activity is also observed for Ir, and, to a smaller extent, for Pd (Fig. S5).

As visible in Figure 3, the cycling behavior in PROX (after CO oxidation cycles) is strongly metal-dependent. While the Pt, Pd, and Ir catalysts stabilize after one or two cycles, the Rh and Ru catalysts are strikingly unstable. In the case of Rh-CeO_2, it is seen (Fig. 3d) that above 200 °C, the CO_2 yield in the first run diminishes from more than 100% (107%) down to 73%, and then gradually decreases as temperature increases (the CO_2 yield superior to 100% is ascribed to (non-poisoning) CO

decomposition on Rh-CeO_2 during the last CO oxidation run, which leads to C combustion during the first PROX run, see Section 4.1). During the subsequent cooling run (run 2), the CO_2 yield is much lower than during run 1 (although the light-off temperature decreases). Afterwards, the CO_2 yield in heating run 3 increases to intermediate values, and decreases again during the final cooling run (4). In any case, methane is produced above 260 °C. In order to check whether this apparently chaotic behavior is due to high-temperature events, the catalyst was reduced at 400 °C in H_2 and submitted to a second series of PROX runs in the RT-200 °C range (see Fig. 3f). After the initial run, the CO_2 yields in the following runs are roughly superimposed, implying that the instability observed in Fig. 3d at low temperature was induced by high-temperature effects (> 200 °C). As compared to Rh-CeO_2, Ru-CeO_2 exhibits a less chaotic cycling behavior, but methane is produced at a temperature as low as 170 °C. However, unlike for Rh, the methane yield does not increase significantly above 220 °C (yield < 10%) and does not depend on the run number. The particular kinetics observed for Rh and Ru catalysts are discussed in the next section.

Pt-CeO_2 is the only catalyst reaching almost 100% CO conversion in PROX (around 140 °C), with a selectivity toward CO_2 close to 100% (Fig. 4, c and d). Interestingly, Pt/Al_2O_3, while inactive below 150 °C, is more CO_2 selective than Pt-CeO_2 above this temperature. Alumina is also a better support than ceria for Pd and Ir in terms of selectivity (Fig. S6). On the opposite, Pd-CeO_2 is the poorest catalyst in terms of CO conversion and selectivity to CO_2, reaching only 5% and 10%, respectively. This was previously ascribed to hydrogen absorption by Pd, leading to preferential formation of water [41–43]. The selectivities of Ir and Rh catalysts show the same trends as the Pt-CeO_2 one. They are relatively high at low temperature but gradually decrease when temperature increases. Nevertheless, the final selectivity of the Rh catalyst is lower than that of Pt and Ir, and exhibits a very chaotic cycling behavior when the catalyst is tested in the full temperature (Fig. S7). If the Rh catalyst operating temperature is limited to the RT-200 °C range (as in the case of Fig. 4b-d), its selectivity to CO_2 is roughly constant at intermediate temperatures (Fig. 4d). Strikingly, Ru-CeO_2 exhibits a selectivity plateau, reaching 50% in the wide 160-260 °C temperature range.

4. Discussion

4.1. CO dissociation and methanation over Rh and Ru catalysts

During the PROX reaction, methane was detected at the reactor outlet at high temperature for all catalysts, but in large amounts only for Rh and Ru catalysts. In the H_2-rich gas streams obtained from

hydrocarbon feedstock reforming, the following reactions can proceed, to different extents, over the catalysts [44]:

CO oxidation:	$CO + ½\ O_2 \rightarrow CO_2$	$\Delta H^\circ = -283$ kJ mol^{-1}	(1)
H_2 oxidation:	$H_2 + ½\ O_2 \rightarrow H_2O$	$\Delta H^\circ = -242$ kJ mol^{-1}	(2)
CO methanation:	$CO + 3H_2 \rightarrow CH_4 + H_2O$	$\Delta H^\circ = -206$ kJ mol^{-1}	(3)
CO_2 methanation:	$CO_2 + 4H_2 \rightarrow CH_4 + 2H_2O$	$\Delta H^\circ = -165$ kJ mol^{-1}	(4)
Water-gas shift and reverse WGS:	$CO + H_2O \leftrightarrow CO_2 + H_2$	$\Delta H^\circ = -41$ kJ mol^{-1}	(5)

For PROX, the catalysts should be preferentially active in reaction 1, and reaction 2 should be avoided. In the case of Ru-based catalysts, CO methanation (reaction 3) was reported to proceed simultaneously to PROX [44,45]. In presence of CO_2-rich environments, CO_2 methanation (reaction 4) may also occur [46]. Ru or Rh supported on alumina and Ru/TiO_2 were shown to be efficient for the selective CO methanation in the presence of CO_2, which was claimed to be a possible alternative to PROX [2,47,48]. Investigating this reaction on Ru/Al_2O_3, Xu *et al*. suggested that, although the strongly adsorbed carbonaceous species issuing from CO decomposition can be reacted off at high temperatures, the deposited carbon deactivates the catalyst at the (lower) temperatures of 100% selective CO methanation [48]. The methanation activity of Ru and Rh catalysts is generally much higher than that of Pd or Pt, which can be related to the smaller CO dissociation barrier on the formers [49,50]. Panagiotopoulou *et al*. indicated that, under pure CO methanation conditions, the selectivity to CH_4 gradually increases with temperature, although higher hydrocarbons are also produced, the selectivity to which decreases with increasing temperature [51] (in our case, C_2 and C_3 hydrocarbons were indeed detected on our Rh-CeO_2 and Ru-CeO_2 catalysts, although in trace amounts). In the presence of water, the catalytic activity of Ru is not affected, while Rh exhibits lower CO conversions, and Pt and Pd mainly promote the conversion of CO to CO_2 via WGS (reaction 5) [51].

Following this quick literature survey, the cyclic behavior of the CO_2 yields observed for Rh-CeO_2 (Fig. 3d) and Ru-CeO_2 (Fig. 3e) could at first sight be analyzed in terms of catalyst deactivation. However, plotting O_2 consumption during the successive PROX runs (Fig. S8) shows that O_2 is fully consumed, with the same light-off temperature whatever the run, above 180°C for Rh (with exception of the first run, 210°C) and 220°C for Ru. Thus, one has to admit that, from a run to the other, the selectivity is more affected (see Fig. S7) than the activity. Moreover, this relative absence of poisoning is consistent with the absence of observed deactivation in H_2-free CO oxidation. At least two explanations can be suggested for the chaotic cycling selectivity of Rh and Ru catalysts during PROX experiments. (i) First,

one can assume that CO decomposes above ca. 170 °C (i.e., when methane is detected), leaving carbon on the metal surface. The major part of this carbon is readily oxidized to CO_2, while the other part is strongly adsorbed on specific surface sites, modifying the catalyst selectivity. The catalyst partly regenerates upon cooling below ca. 200 °C, temperatures at which CO no longer dissociates and adsorbed carbon is oxidized by oxygen. Thus, the catalyst regains its initial selectivity at low temperature, and its CO oxidation activity decreases again at high temperature in favor of H_2 oxidation. In addition, above ca. 170 °C for Ru and ca. 260 °C for Rh, some carbon reacts with H_2 to form methane (Fig. 3, d and e). (ii) Second, the oxidation states of Rh and Ru are expected to be very sensitive to the reaction conditions (and, in addition, to the presence of the highly reducible ceria support). Indeed, various studies suggest that surface oxides on transition metal nanoparticles, in particular Rh and Ru, play an important role in determining the CO oxidation activity [52–55]. Hence, in our case, rather slow metal oxidation and oxide reduction kinetics under PROX atmosphere throughout heating and cooling runs could be at the origin of the apparently random cyclic behavior of Rh-CeO_2 and Ru-CeO_2. Anyhow, this aspect would deserve further investigation.

4.2. Activity trends

For H_2-free CO oxidation on single-crystal surfaces, Goodman and Peden have found that Ru is more active than Rh [56], and that Pd and Ir are more active than Pt [57]. Some of us have shown that Ir is more active than Pt, both without and with hydrogen [58]. Our present results on ceria-supported PGMs (TOF order: Rh > Pd > Pt > Ru > Ir, Fig. 4b) are not consistent with these works on extended surfaces, but agree well with the trends observed for alumina and ceria-supported Rh, Pd and Pt [5]. This underlines the influence of metal nanoparticle size and structure in CO oxidation [59].

In comparison to H_2-free CO oxidation, the light-off temperatures for CO oxidation under PROX conditions are shifted by -30° C for Ru and by up to -120 °C for Pt, whereas no shift is observed for Rh catalysts. Thus, the H_2 boosting effect is metal-dependent and the resulting PROX TOF order is: Pt > Pd > Rh > Ir > Ru (Fig. 4b). The promoting effect of H_2 on CO oxidation was already observed by several groups in the case of Pt [60,61]. Two important results from the literature must be recalled to explain the present results. (i) First, Eichhorn and coworkers studied both experimentally and theoretically the PROX reactivity of core-shell M@Pt nanoparticles (M = Ru, Rh, Ir, Pd, Au), and proposed a H-mediated O_2 dissociation mechanism [62,63]: H* addition to O_2* leads to low-energy-barrier formation of a hydroperoxy intermediate (O_2H*), which readily decomposes into O* and OH* species (* denotes adsorbed species). The authors suggest that, in H_2-rich PROX environments, surface O* is primarily and very easily generated through this mechanism. For PROX on gold catalysts, we had previously

suggested that hydroperoxy OOH* species could be the critical oxidizing intermediates [64], and a comprehensive mechanism of this promotion was proposed [65]. (ii) Second, Falsig *et al*. calculated from DFT the CO* + O* reaction activation energy for H_2-free CO oxidation on various fcc (111) metal surfaces, showing that this step is much less activated on Pt and Pd than on Ru and Rh [66]. Moreover, for the same reaction step on PGM (reduced or oxidized) close-packed surfaces, Gong *et al*. [52] predicted exactly the same trend as we find for PROX. Combining these published results, it is clear that in the presence of H_2, O* atoms are easily available on the metal surface and react much more readily on Pt and Pd than on Ir, Rh and Ru.

Obviously, the present explanation only focuses on intrinsic metallic effects and does not include additional possible phenomena involving the ceria support, which can supply activated oxygen atoms to the metals via a Mars van Krevelen mechanism [67]. Various groups have shown the critical influence of the support on the PROX performances, which is general positive in the case of ceria or/and zirconia with respect to alumina [5–8,68]. Here, by comparing alumina and ceria supports for Pt, Ir and Pd, we indeed observe a considerable enhancement of the CO oxidation activity induced by ceria, especially in the presence of H_2 for Pt and Ir catalysts. When supported on alumina, Ru has been found superior to Pt by several authors [11,44,45], but prone to also catalyze CO methanation, as already mentioned. Moreover, the sensitivity of the PGM (and Ce) oxidation state to the (H_2-free or H_2-rich) atmosphere is likely to play a role in the reaction-dependent activity trends. For example, in the case of Rh, whether reduced Rh or RhO_x is the (most) active phase in CO oxidation has been intensively debated [54,69].

5. Conclusions

CO oxidation ($CO:O_2$ 2:2% in He, 1 atm) and PROX ($CO:O_2:H_2$ 2:2:48%) were investigated from RT to 400 °C on ca. 1 wt% Pt, Pd, Ir, Rh, and Ru supported on ceria. The catalysts were synthesized in one step by solution combustion using the glycine-nitrate process.

As shown by aberration-corrected HRTEM, all the catalysts exhibit a similar puzzle-like structure with round macropores and flat mesopores. The ceria crystallite and metal particle sizes are in the 20-40 nm and 2-6 nm ranges, respectively. CO-DRIFTS experiments show that, apart from Ru-CeO_2, the fresh samples adsorb much less CO than those pre-reduced *in situ* at 400 °C in H_2 flow. This means that the metals are initially oxidized and possibly partly dispersed in the ceria matrix.

However, the as-prepared catalysts are all active and stable in CO oxidation, without pre-reduction, and an *in situ* reduction in H_2 does not significantly affect the reaction rates. The CO oxidation TOFs

established in the light-off region follow the order: Rh > Pd > Pt > Ru > Ir. Upon addition of hydrogen (PROX), a metal-dependent change in the CO oxidation rate is observed. The TOF of Rh moderately decreases, while it increases for all other metals. The highest H_2-induced boost is observed for Pt-CeO_2, the light-off temperature decreasing by 120 °C. As a result, the CO-PROX TOF order is: Pt > Pd > Rh > Ir > Ru. This sequence exactly matches the trends in CO*+O* activation energy predicted by DFT calculations, which thereby confirms that (i) hydrogen facilitates the activation of O_2 into O*, and (ii) the CO*+O* step is rate-determining in PROX.

The ceria-supported SCS catalysts were compared to alumina-supported catalysts prepared by impregnation, showing that (i) for every metal (Pt, Pd, Ir), ceria is beneficial to CO oxidation and PROX activities; (ii) the nature and extent of H_2 effect on CO oxidation is not only metal-dependent but also support-dependent.

In terms of selectivity toward CO_2, Pt-CeO_2 is the most efficient system below 160 °C, and reaches 100% selectivity near 100 °C. Above 160 °C, Ru is the most selective ceria-supported catalyst (ca. 45% CO_2) but the least active one. However, the interest of ceria is limited at these high temperatures, since the alumina-supported Pt, Pd and Ir catalysts appear more selective than the ceria-supported ones.

Finally, the Rh and Ru systems also catalyze CO dissociation and methanation at these temperatures, and show high instabilities in the CO_2 yields during the heating/cooling cycles. These chaotic behaviors are ascribed to (i) temperature-dependent CO dissociation and combustion of the resulting carbonaceous species or/and (ii) oxidation/reduction of the surface RhO_x and RuO_x phases, leading to deactivation/regeneration cycles and changes in CO_2 selectivity.

Acknowledgements

We acknowledge the French National Research Agency for funding through the ANR-BS10-009 “DINAMIC” project, the CLYM for access to the FEI Titan microscope, and the European COST Action CM1104 “Red ox” for networking discussions. L. Burel (conventional TEM), N. Cristin & P. Mascunan (ICP, BET) and Y. Aizac (XRD) are greatly thanked for technical support.

References

[1] N. Bion, F. Epron, M. Moreno, F. Mariño, D. Duprez, Top. Catal. 51 (2008) 76-88.
[2] E.D. Park, D. Lee, H.C. Lee, Catal. Today 139 (2009) 280-290.
[3] K. Liu, A. Wang, T. Zhang, ACS Catal. 2 (2012) 1165-1178.

[4] A. Trovarelli, P. Fornasiero, Catalysis by Ceria and Related Materials: 2nd Edition, Imperial College Press, 2013.
[5] T. Bunluesin, E.S. Putna, R.J. Gorte, Catal. Lett. 41 (1996) 1-5.
[6] F. Mariño, C. Descorme, D. Duprez, Appl. Catal. B 54 (2004) 59-66.
[7] Y. Huang, A. Wang, X. Wang, T. Zhang, Int. J. Hydrogen Energy 32 (2007) 3880-3886.
[8] A. Wootsch, C. Descorme, D. Duprez, J. Catal. 225 (2004) 259-266.
[9] C. Galletti, S. Specchia, G. Saracco, V. Specchia, Ind. Eng. Chem. Res. 47 (2008) 5304-5312.
[10] X. Chen, J.J. Delgado, J.M. Gatica, S. Zerrad, J.M. Cies, S. Bernal, J. Catal. 299 (2013) 272-283.
[11] S.H. Oh, R.M. Sinkevitch, J. Catal. 142 (1993) 254-262.
[12] S.L. González-Cortés, F.E. Imbert, Appl. Catal. A 452 (2013) 117-131.
[13] M.S. Hegde, G. Madras, K.C. Patil, Acc. Chem. Res. 42 (2009) 704-712.
[14] S. Colussi, A. Gayen, M. Farnesi Camellone, M. Boaro, J. Llorca, S. Fabris, A. Trovarelli, Angew. Chem. Int. Ed. 48 (2009) 8481-8484.
[15] T.S. Nguyen, G. Postole, S. Loridant, F. Bosselet, L. Burel, M. Aouine, L. Massin, F. Morfin, P. Gélin, L. Piccolo, J. Mater. Chem. A 2 (2014) 19822-19832.
[16] S.R. Jain, K.C. Adiga, V.R. Pai Verneker, Combust. Flame 40 (1981) 71-79.
[17] G. Postole, T.S. Nguyen, M. Aouine, P. Gélin, L. Cardenas, L. Piccolo, Appl. Catal. B 10.1016/j.apcatb.2014.11.024 (2014).
[18] K.S.W. Sing, D.H. Everett, R.A.W. Haul, L. Moscou, R.A. Pierotti, J. Rouquérol, T. Siemieniewska, Pure Appl. Chem. 57 (1985) 603-619.
[19] R.D. Shannon, Acta Cryst. A 32 (1976) 751-767.
[20] S. Alayoglu, K. An, G. Melaet, S. Chen, F. Bernardi, L.W. Wang, A.E. Lindeman, N. Musselwhite, J. Guo, Z. Liu, M.A. Marcus, G.A. Somorjai, J. Phys. Chem. C 117 (2013) 26608-26616.
[21] T.S. Nguyen, F. Morfin, L. Piccolo, In Preparation.
[22] C. Li, Y. Sakata, T. Arai, K. Domen, K. Maruya, T. Onishi, J. Chem. Soc., Faraday Trans. 1 85 (1989) 929-943.
[23] T. Jin, Y. Zhou, G.J. Mains, J.M. White, J. Phys. Chem. 91 (1987) 5931-5937.
[24] D.W. Daniel, J. Phys. Chem. 92 (1988) 3891-3899.
[25] A. Holmgren, B. Andersson, D. Duprez, Appl. Catal. B 22 (1999) 215-230.
[26] P. Bazin, O. Saur, J.C. Lavalley, M. Daturi, G. Blanchard, Phys. Chem. Chem. Phys. 7 (2005) 187-194.
[27] J. Szanyi, W.K. Kuhn, D.W. Goodman, J. Vac. Sci. Technol. A 11 (1993) 1969-1974.
[28] M. Fernández-García, A. Martínez-Arias, L.N. Salamanca, J.M. Coronado, J.A. Anderson, J.C. Conesa, J. Soria, J. Catal. 187 (1999) 474-485.
[29] R.W. Boyle, J. Lauterbach, M. Schick, W.J. Mitchell, W.H. Weinberg, Ind. Eng. Chem. Res. 35 (1996) 2986-2992.
[30] A. Erdohelyi, K. Fodor, G. Suru, Appl. Catal. A 139 (1996) 131-147.
[31] U. Nylén, L. Sassu, S. Melis, S. Järås, M. Boutonnet, Appl. Catal. A 299 (2006) 1-13.
[32] J.T. Yates, K. Kolasinski, J. Chem. Phys. 79 (1983) 1026-1030.
[33] L. Basini, M. Marchionna, A. Aragno, J. Phys. Chem. 96 (1992) 9431-9441.
[34] A. Martínez-Arias, J. Soria, J.C. Conesa, J. Catal. 168 (1997) 364-373.
[35] G.H. Yokomizo, C. Louis, A.T. Bell, J. Catal. 120 (1989) 1-14.
[36] C.H.F. Peden, F.M. Hoffmann, Catal. Lett. 10 (1991) 91-101.
[37] K. Hadjiivanov, J.-C. Lavalley, J. Lamotte, F. Maugé, J. Saint-Just, M. Che, J. Catal. 176 (1998) 415-425.
[38] W. Xu, R. Si, S.D. Senanayake, J. Llorca, H. Idriss, D. Stacchiola, J.C. Hanson, J.A. Rodriguez, J. Catal. 291 (2012) 117-126.
[39] G. Bergeret, P. Gallezot, in: Handbook of Heterogeneous Catalysis, VCH, G. Ertl, H. Knözinger, J. Weitkamp (Eds.), Weinheim, 1997.
[40] L. Piccolo, S. Nassreddine, M. Aouine, C. Ulhaq, C. Geantet, J. Catal. 292 (2012) 173-180.
[41] F. Morfin, S. Nassreddine, J.L. Rousset, L. Piccolo, ACS Catal. 2 (2012) 2161-2168.

[42] O. Pozdnyakova-Tellinger, D. Teschner, J. Krohnert, F.C. Jentoft, A. Knop-Gericke, R. Schlogl, A. Wootsch, J. Phys. Chem. C 111 (2007) 5426-5431.
[43] C. Zlotea, F. Morfin, T.S. Nguyen, N.T. Nguyen, J. Nelayah, C. Ricolleau, M. Latroche, L. Piccolo, Nanoscale 6 (2014) 9955-9959.
[44] Y.H. Kim, E.D. Park, H.C. Lee, D. Lee, K.H. Lee, Catal. Today 146 (2009) 253-259.
[45] D.J. Suh, C. Kwak, J.-H. Kim, S.M. Kwon, T.-J. Park, J. Power Sources 142 (2005) 70-74.
[46] A. Trovarelli, C. Deleitenburg, G. Dolcetti, J.C.S. Araujo, J. Llorca, J. Catal. 151 (1995) 111-124.
[47] P. Djinović, C. Galletti, S. Specchia, V. Specchia, Catal. Today 164 (2011) 282-287.
[48] G. Xu, X. Chen, Z.-G. Zhang, Chem. Eng. J. 121 (2006) 97-107.
[49] Z.-P. Liu, P. Hu, J. Chem. Phys. 114 (2001) 8244-8247.
[50] S. Wang, B. Temel, J. Shen, G. Jones, L.C. Grabow, F. Studt, T. Bligaard, F. Abild-Pedersen, C.H. Christensen, J.K. Nørskov, Catal. Lett. 141 (2011) 370-373.
[51] P. Panagiotopoulou, D.I. Kondarides, X.E. Verykios, Appl. Catal. A 344 (2008) 45-54.
[52] X.-Q. Gong, Z.-P. Liu, R. Raval, P. Hu, J. Am. Chem. Soc. 126 (2004) 8-9.
[53] J. Aßmann, D. Crihan, M. Knapp, E. Lundgren, E. Löffler, M. Muhler, V. Narkhede, H. Over, M. Schmid, A.P. Seitsonen, P. Varga, Angew. Chem. Int. Ed. 44 (2005) 917-920.
[54] J. Gustafson, R. Westerström, O. Balmes, A. Resta, R. van Rijn, X. Torrelles, C.T. Herbschleb, J.W.M. Frenken, E. Lundgren, J. Phys. Chem. C 114 (2010) 4580-4583.
[55] S. Kim, K. Qadir, S. Jin, A. Satyanarayana Reddy, B. Seo, B.S. Mun, S.H. Joo, J.Y. Park, Catal. Today 185 (2012) 131-137.
[56] D.W. Goodman, C.H.F. Peden, J. Phys. Chem. 90 (1986) 4839-4843.
[57] P.J. Berlowitz, C.H.F. Peden, D.W. Goodman, J. Phys. Chem. 92 (1988) 5213-5221.
[58] L. Piccolo, S. Nassreddine, F. Morfin, Catal. Today 189 (2012) 42-48.
[59] L. Piccolo, in: Nanoalloys: Synthesis, Structure and Properties, D. Alloyeau, C. Mottet, C. Ricolleau (Eds.), Springer-Verlag, London, 2012.
[60] M. Kahlich, H.A. Gasteiger, R.J. Behm, J. Catal. 171 (1997) 93-105.
[61] S. Salomons, R.E. Hayes, M. Votsmeier, Appl. Catal. A 352 (2009) 27-34.
[62] S. Alayoglu, A.U. Nilekar, M. Mavrikakis, B. Eichhorn, Nat. Mater. 7 (2008) 333-338.
[63] A.U. Nilekar, S. Alayoglu, B. Eichhorn, M. Mavrikakis, J. Am. Chem. Soc. 132 (2010) 7418-7428.
[64] C. Rossignol, S. Arrii, F. Morfin, L. Piccolo, V. Caps, J.L. Rousset, J. Catal. 230 (2005) 476-483.
[65] E. Quinet, L. Piccolo, F. Morfin, P. Avenier, F. Diehl, V. Caps, J.L. Rousset, J. Catal. 268 (2009) 384-389.
[66] H. Falsig, B. Hvolbæk, I.S. Kristensen, T. Jiang, T. Bligaard, C.H. Christensen, J.K. Nørskov, Angew. Chem. Int. Ed. 47 (2008) 4835-4839.
[67] S. Royer, D. Duprez, ChemCatChem 3 (2011) 24-65.
[68] M.M.V.M. Souza, N.F.P. Ribeiro, M. Schmal, Int. J. Hydrogen Energy 32 (2007) 425-429.
[69] F. Gao, Y. Cai, K.K. Gath, Y. Wang, M.S. Chen, Q.L. Guo, D.W. Goodman, J. Phys. Chem. C 113 (2009) 182-192.

Table 1. Characteristics of the samples.

Sample name	***Metal content (wt%)[a]***	***Metal particle size (nm) Fresh / Reduced***	***Mean ceria crystallite size / lattice parameter (nm)[c]***	***Surface area (m^2/g)[d]***
CeO_2	0	-	24 / 0.54134	28
Pt-CeO_2	0.98	ND / 4.0 ± 1.3	27 / 0.54123	17
Pd-CeO_2	0.31	ND / 6.5 ± 1.9	27 / 0.54137	35
Ir-CeO_2	0.93	2.1 ± 0.7 / 3.4 ± 1.1	26 / 0.54147	29
Rh-CeO_2	0.73	4.6 ± 1.8 / 4.7 ± 1.5	39 / 0.54136	12
Ru-CeO_2	1.01	2.8 ± 1.1 / 3.1 ± 1.3	23 / 0.54138	20

[a] Determined by ICP-OES; [b] Determined by TEM (the "reduced" samples were heated to 400 °C in H_2 flow) ; [c] Determined by XRD Rietveld refinements for as-prepared catalysts; [d] Determined by N_2 adsorption volumetry (BET) for as-prepared catalysts. ND = not determined

Table 2. Apparent activation energies.

Sample name	***Activation energy (kJ/mol) in CO oxidation***	***Activation energy (kJ/mol) in CO PROX***
Pt-CeO_2	59 ± 1	83 ± 2
Pd-CeO_2	45 ± 2	59 ± 1
Ir-CeO_2	83 ± 2	70 ± 1
Rh-CeO_2	70 ± 1	77 ± 1
Ru-CeO_2	90 ± 3	92 ± 1

Figure 1. Electron micrographs of as-prepared Pt-CeO_2 (a-c), reduced Pd-CeO_2 (d-f), and reduced Rh-CeO_2 (g-i). Image (a) was recorded in STEM-HAADF mode, while all the other images were acquired in TEM mode.

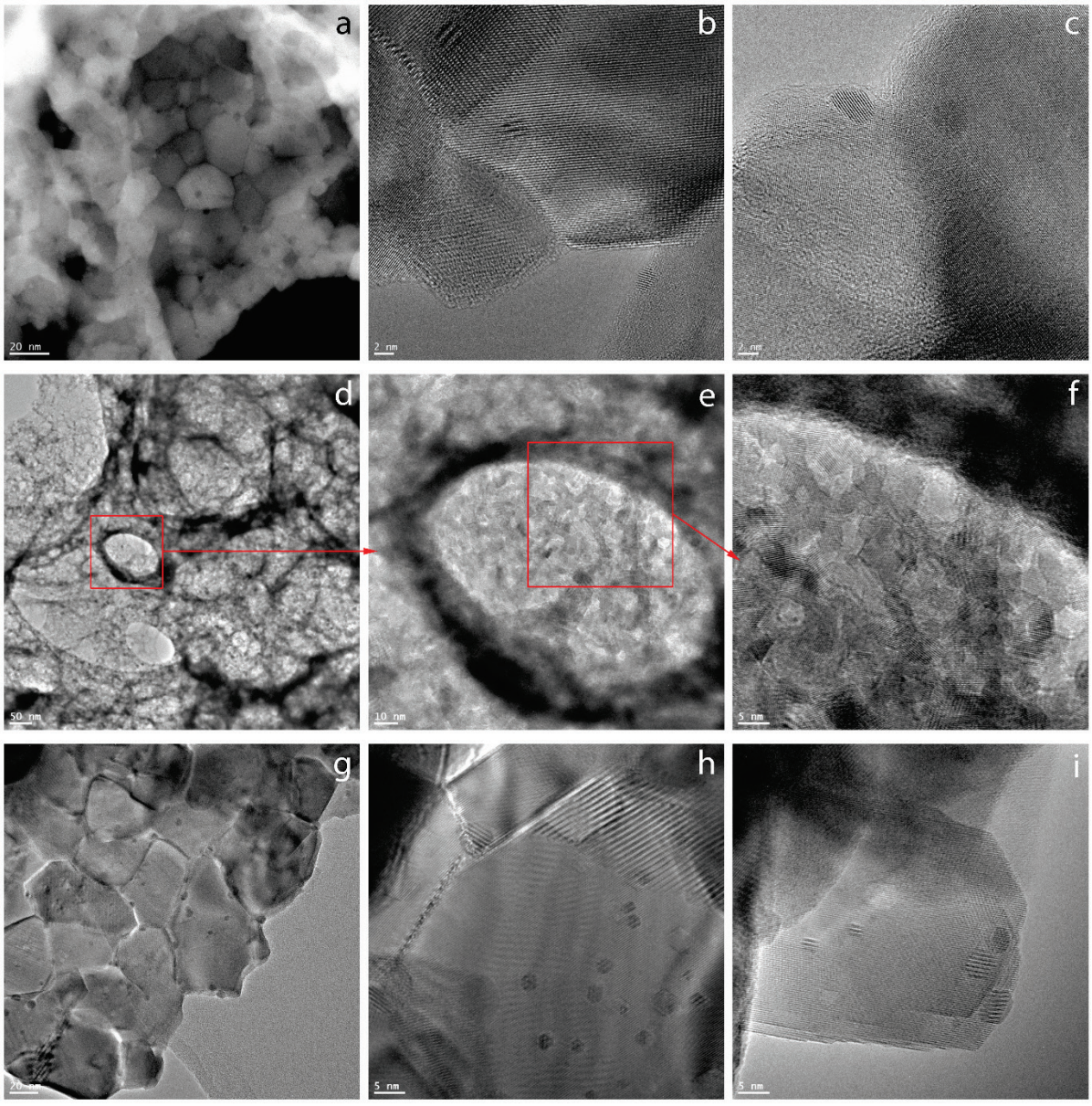

Figure 2. DRIFT spectra of adsorbed CO measured at 50 °C on fresh and *in situ* reduced catalysts.

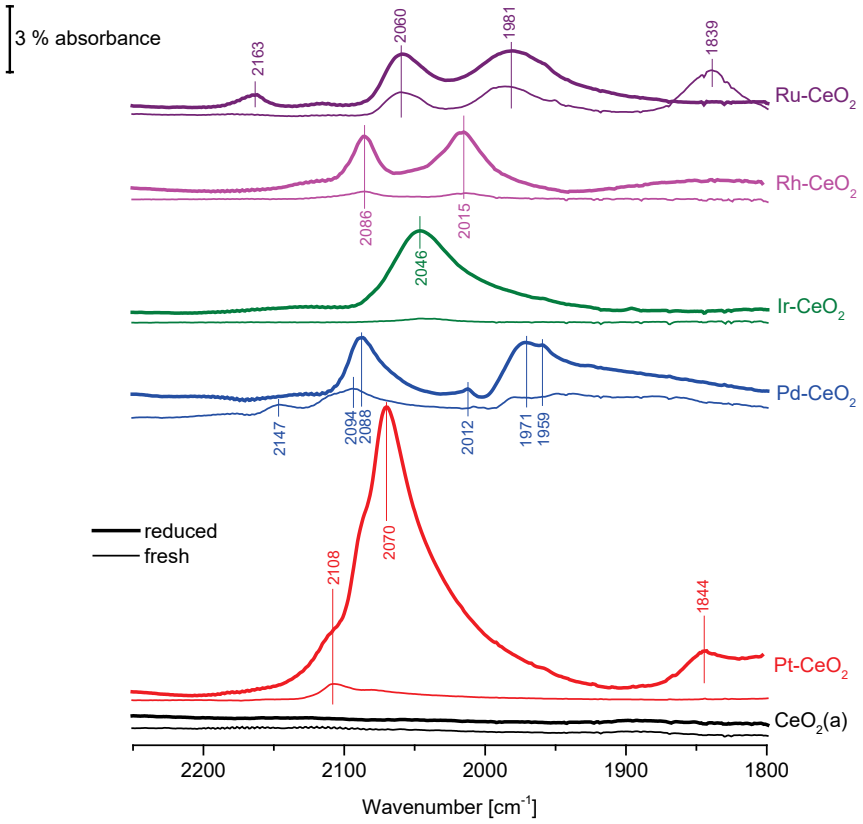

Figure 3. CO_2 and CH_4 yields during the whole sequence of CO oxidation and PROX reaction runs on each PGM-CeO_2 catalyst. Methane formation is negligible for Pt, Pd, and Ir catalysts.

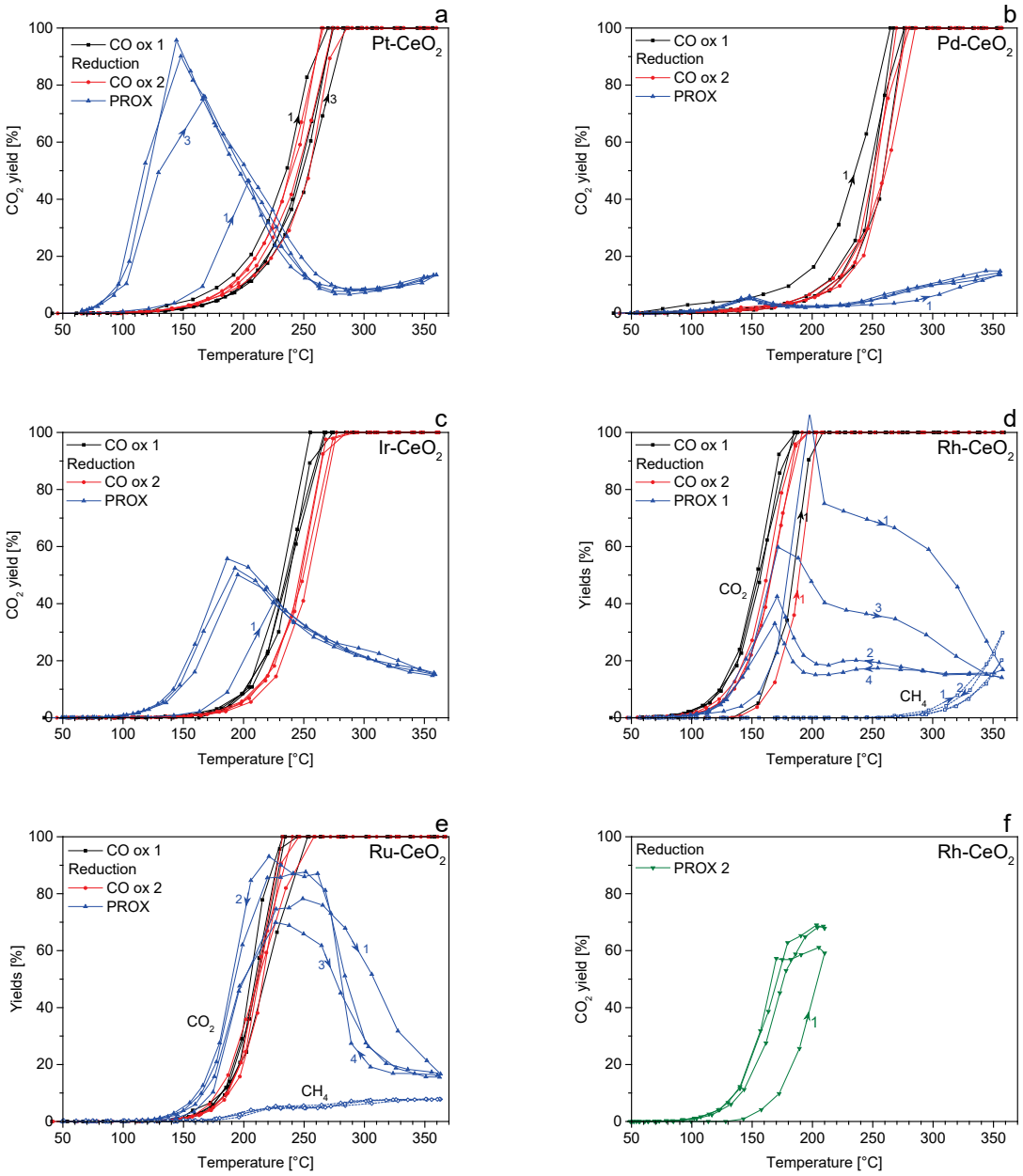

Figure 4. (a) CO_2 yield versus temperature in CO oxidation. (b) Arrhenius plots of CO_2 turnover frequency in CO oxidation and PROX. (c) CO_2 yield versus temperature in PROX. (d) Selectivity to CO_2 in PROX. The data for a reference Pt/Al_2O_3 catalyst are reported (a, c, d) for comparison.